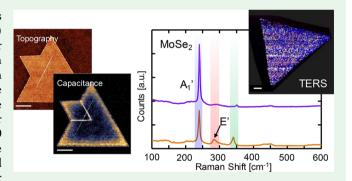# Nanoscale Heterogeneities in Monolayer MoSe₂ Revealed by Correlated Scanning Probe Microscopy and Tip-Enhanced Raman Spectroscopy

Kirby K. H. Smithe,[†,O] Andrey V. Krayev,[‡,O] Connor S. Bailey,[†] Hye Ryoung Lee,[†,§] Eilam Yalon,[†] Özgür Burak Aslan,[∥,⊥] Miguel Muñoz Rojo,[†] Sergiy Krylyuk,[#] Payam Taheri,[#] Albert V. Davydov,[#] Tony F. Heinz,[∥,⊥] and Eric Pop*[,†,§,∇]

[†]Department of Electrical Engineering, Stanford University, Stanford, California 94305, United States

[‡]Horiba Scientific, Novato, California 94949, United States

[§]Department of Materials Science & Engineering, Stanford University, Stanford, California 94305, United States

[∥]Department of Applied Physics, Stanford University, Stanford, California 94305, United States

[⊥]SLAC National Accelerator Laboratory, Menlo Park, California 94025, United States

[#]Material Measurement Laboratory, National Institute of Standards and Technology, Gaithersburg, Maryland 20899, United States

[∇]Precourt Institute for Energy, Stanford University, Stanford, California 94305, United States

S *Supporting Information*

ABSTRACT: Understanding growth, grain boundaries (GBs), and defects of emerging two-dimensional (2D) materials is key to enabling their future applications. For quick, nondestructive metrology, many studies rely on confocal Raman spectroscopy, the spatial resolution of which is constrained by the diffraction limit (∼0.5 μm). Here we use tip-enhanced Raman spectroscopy (TERS) for the first time on synthetic MoSe₂ monolayers, combining it with other scanning probe microscopy (SPM) techniques, all with sub-20 nm spatial resolution. We uncover strong nanoscale heterogeneities in the Raman spectra of MoSe₂ transferred to gold substrates [one near 240 cm⁻¹ (A₁′), and others near

287 cm⁻¹ (E′), 340 cm⁻¹, and 995 cm⁻¹], which are not observable with common confocal techniques and appear to imply the presence of nanoscale domains of MoO₃. We also observe strong tip-enhanced photoluminescence (TEPL), with a signal nearly an order of magnitude greater than the far-field PL. Combining TERS with other SPM techniques, we find that GBs can cut into larger domains of MoSe₂, and that carrier densities are higher at GBs than away from them.

KEYWORDS: *tip-enhanced Raman spectroscopy, scanning probe microscopy, chemical vapor deposition, MoSe₂, heterogeneity*

■ INTRODUCTION

Two-dimensional (2D) semiconductors, specifically the class of monolayer (1L) transition metal dichalcogenides (TMDs), have attracted significant attention in recent years due to their unique electrical, thermal, and optical properties. These include direct optical band gaps in the visible to near-infrared wavelengths,[1−3] valley-specific circular dichroism,[4−7] and strong excitonic interactions even at room temperature.[8−12] Among 2D materials, monolayer MoSe₂ is known to have a direct optical band gap around 1.55 eV,[13−17] and devices with mobility values somewhat higher than the more prevalently studied MoS₂ have been reported,[18−20] making this material an attractive candidate for nano- and optoelectronic applications.

Nonetheless, most research on 2D TMDs to date has focused on characterization techniques that measure properties on the scale of microns or larger, including X-ray photo-emission spectroscopy (XPS), far-field photoluminescence (PL) and confocal Raman spectroscopy, as well as micro-electronic device measurements. However, devices in modern electronics tend to be smaller than ∼100 nm, and as such it is critical to employ techniques that allow for (preferably nondestructive) characterization on the order of tens of nanometers.[21]

Imaging with tip-enhanced Raman spectroscopy (TERS) is a natural choice for comprehensive nanoscale characterization technique for 2D materials, because it combines the advantages of strong enhancement of the Raman signal by a plasmonic structure located at the apex of a scanning probe microscope tip
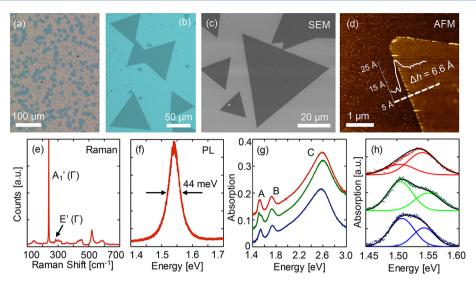
Figure 1. (a, b) Optical images of large-grain, single crystal, monolayer MoSe$_2$ grown by CVD on SiO$_2$/Si substrates. (c) SEM image of similar MoSe$_2$ single crystals. (d) AFM scan on the edge of a flake, demonstrating a monolayer step height $\Delta h <$ 7 Å and RMS roughness on the crystal surface of 1.6 Å. (e) Confocal Raman spectrum of 1L MoSe$_2$ taken with a 532 nm laser, with the characteristic A$_1'$ peak at 239 cm^{-1} and overtones at higher energies. (f) Far-field PL of monolayer MoSe$_2$, showing a direct optical band gap of 1.53 eV and full-width at half-maximum (fwhm) of 43.8 meV. (g) Three absorption spectra on different areas of a similar MoSe$_2$ crystal grown directly on quartz and adjusted to reflect absorption for free-standing samples (offset for clarity). (h) Zoomed-in view of absorption around the A exciton with background subtracted, emphasizing the broadening and splitting of this feature. Two Gaussian curves are required to fit each feature, indicating spatial inhomogeneity in regions smaller than a few hundred nanometers.

with high spatial resolution (down to a few nm) of both the hyperspectral Raman maps and multiple scanning probe microscopy (SPM) channels such as topography, phase shift, surface potential, conductivity, etc. Recent advances in development of efficient SPM systems with dedicated TERS imaging modes[22] have enabled nanoscale characterization of novel 2D materials, both carbon-based[23−25] and TMDs, first for nanoscale tip-enhanced PL (TEPL) imaging[26−28] and then for TERS imaging of mono-to-few-layer MoS$_2$[29−31] and WS$_2$.[32] Many of these initial studies revealed interesting nanoscale inhomogeneities in the optical and vibrational properties of 2D materials which could not be observed or properly characterized with conventional techniques.

To this end, we perform TERS measurements of 1L polycrystalline MoSe$_2$ films synthesized by chemical vapor deposition (CVD) and transferred to gold substrates. Optical spectroscopy, Raman scattering, photoluminescence (PL), contact potential difference (CPD), and $\partial^2 C/\partial z^2$ (capacitance) measurements are all performed with a resolution below 20 nm. We demonstrate that cross-correlating the results provided by scanning Kelvin probe microscopy (SKPM) and these other tip-enhanced techniques can yield important information on the unexpected spatial distributions of grain boundaries in polycrystalline MoSe$_2$ flakes. On one hand, we observe increased capacitance at the grain boundaries of MoSe$_2$ as-grown on SiO$_2$/Si, but a sharply decreased capacitance and TERS signal at the grain boundaries of flakes transferred to Au substrates. Based on the observations, we argue that the concentration of the charge carriers in these boundaries is increased compared to the interior of the as-grown monolayer crystals, but that exposure to base solutions for transferring etches the crystal at the grain boundaries. We also find that, even in monocrystalline flakes, there exist small (20−100 nm) domains with Raman signatures different from the rest of the transferred flake, with the TERS spectra in the nanoscale regions implying the presence of MoO$_3$. This work highlights
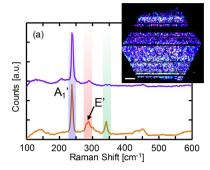
the importance of nanoscale characterization of 2D materials and also demonstrates the capability of simultaneous combined scanning probe techniques to meet this need.

■ SAMPLE FABRICATION

We synthesize 1L MoSe$_2$ crystals by chemical vapor deposition (CVD) using a 2 in. tube furnace system from planarTECH. (A diagram, photograph, and specific preparation steps are presented in the Supporting Information section A.) The MoSe$_2$ is grown with the aid of a perylene-3,4,9,10 tetracarboxylic acid tetrapotassium salt (PTAS) solution[33] distributed over the surface of SiO$_2$/Si substrates in a manner very similar to that in ref 34. The growths are initially characterized by optical and scanning electron microscopy (SEM), which reveal grain sizes ranging from a few μm to 100 μm on an edge (see Figure 1a−c) and grown covering an area of several cm^2. We also initially confirm the 1L nature of the crystals with atomic force microscopy (AFM), shown in Figure 1d. It is worth noting that, in addition to a measured step height of ∼0.66 nm, the root-mean-square roughness of the flake is merely 0.16 nm, suggesting that the surface is atomically smooth.

Further characterization is performed by room-temperature confocal Raman and far-field PL measurements using a 532 nm laser with ∼1 μm spot size, shown in Figure 1e,f. Similar to previous reports,[13,16] we observe a strong A$_1'$ peak at 239.4 cm^{-1}, as well as many other weaker peaks and overtones at higher wavenumbers. The prominent PL peak, indicative of a direct band gap in monolayer TMDs,[35] is centered at 1.53 eV with a line width of 43.8 meV. We also characterize our as-grown films with X-ray photoelectron spectroscopy (XPS, see the Supporting Information section B), and find the Mo 3d$_{3/2}$ and 3d$_{5/2}$ peaks to be centered at 232 and 229 eV, indicating that all the Mo is bonded as Mo^{4+} (these peaks blueshift by ∼4 eV for Mo^{6+}).[18,36] Analogous peaks for Se are also shown as the doublet centered around 55 eV.

Finally, we perform optical absorption measurements of MoSe$_2$ grown directly on quartz (Figure 1g), which reveal three strong excitonic features near 1.53, 1.73, and 2.59 eV, respectively, corresponding to the A, B, and C excitons. The 200 meV splitting of the A and B excitons is consistent with previous reports.[37] It is worth noting that the PL and absorption peaks are slightly redshifted
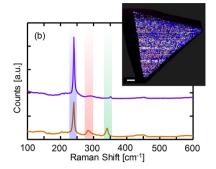
Figure 2. (a) Combined TERS spectra of a polycrystalline monolayer MoSe$_2$ flake transferred to gold, collected with a shorter focal distance Raman spectrometer (XPlora). Intensity of three different peaks are illustrated by color: ~240 cm^{-1} (blue), ~287 cm^{-1} (red), and ~340 cm^{-1} (green). Two distinct types of Raman spectra are observed: nonresonant (purple) with a single dominant peak at 240 cm^{-1}; and resonant (orange) with significant intensity of peaks at 287 and 340 cm^{-1} as well as broad overtones between 400 and 600 cm^{-1}. Inset: TERS map of the polycrystalline flake. The horizontal dark lines in the TERS image are the result of the probe picking up some contamination and losing the enhancement as a consequence; however, even with these imperfections, the pattern of the grain boundaries (GBs) is clearly discernible. (b) Similar combined TERS spectra of a monocrystalline monolayer MoSe$_2$ flake on gold collected with a LabRam-EVO Raman spectrometer. Inset: TERS map of the monocrystalline flake. Scale bars are 1 μm.

relative to reports for exfoliated flakes due to the CVD-grown films experiencing tensile strain during cooling after synthesis.[38] For absorption spectra taken at different locations, we observe slightly different relative values of splitting and broadening in the excitonic peaks, emphasized with peak fitting in Figure 1h. Given that our laser spot size is several hundred nm for these measurements, we can conclude that nanoscale domains with differing properties exist on the scale of a few hundred nm; however, detailed characterization of these domains requires further measurement techniques coupled with scanning probe microscopy, as detailed below.

■ NANOSCALE CHARACTERIZATION

Nanoscale characterization of synthesized monolayer MoSe$_2$ films was performed with scanning probe microscopy (SPM) and tip-enhanced optical spectroscopy (TEOS), which includes TERS and TEPL. (A diagram of our instrumentation is given in the Supporting Information section C.) Due to the extreme focusing of incoming optical fields by a plasmonic structure at the apex of a TEOS-active SPM microscope (typically several nm and only fundamentally limited by the size of the surface plasmon[39]), the spatial resolution of Raman and PL maps is dramatically improved, far beyond the diffraction limit of conventional confocal microscopy. Additionally, when a full spectrum is collected in every pixel of a scanned map (<20 nm/pixel in most of the TEOS maps presented here), the hyperspectral nature of TEOS imaging permits one to perform detailed analysis of the intensity distribution of any observed feature, as we demonstrate below.

In order to significantly enhance the various TEOS signals, measurements are performed in the gap-mode,[40] whereby a sample is sandwiched between a plasmonic tip and a matching plasmonic substrate (typically silver or gold).[41,42] To enable this type of measurement, MoSe$_2$ samples are transferred from the SiO$_2$ growth substrates to substrates coated with 50 nm of gold, using hot NaOH and a rigid PMMA layer to avoid cracking or wrinkling of the MoSe$_2$ during transfer. (The details of this transfer process can be found in the Supporting Information section D.) SPM and TEOS measurements were performed using an OmegaScope-R (formerly AIST-NT, now Horiba Scientific) coupled either to an XPlora or a LabRam-EVO Raman spectrometer (both from Horiba Scientific), with a laser excitation, respectively, at 638 or 632.8 nm and with power of ~75 μW. OMNI-TERS probes (APP Nano) were

used in all the experiments for both the SPM and TEOS analysis.

We performed TERS measurements on both poly- (Figure 2a) and monocrystalline (Figure 2b) MoSe$_2$ in order to explore possible differences in these morphologies. In both cases, our measurements reveal two distinct types of TERS spectra: a nonresonant spectrum, with a single dominant peak at 240 cm^{-1} (the A$_1'$ mode); and a much more abundant resonant spectrum, where in addition to the 240 cm^{-1} peak, reasonably intense peaks at 287 cm^{-1} (E$'$ mode) and 340 cm^{-1} as well as complex broad peaks at ~430 and 585 cm^{-1} (overtone peaks) are present. All observed peaks are in good agreement with ref 43 except for that at 340 cm^{-1}, which appears to be unreported in the literature for MoSe$_2$. The TERS maps (insets in Figure 2a,b) show that the ratio of the intensities of contributing peaks, represented by color, changes across the sample, implying the presence of nanoscale heterogeneity, discussed further below.

The presence of both types of spectra in the maps is not a mere temporal fluctuation of TERS response and can be reproduced across multiple scans, even though the domains with corresponding type of Raman response were fairly small, on the order of few tens of nanometers across (see the Supporting Information section E). The size of the areas with nonresonant spectra, rarely over 150 nm, makes it essentially impossible to detect such heterogeneity with conventional Raman microscopy, since the observed heterogeneity would be averaged over the laser spot size. The subdiffraction spatial resolution of TERS allows one to see differences in adjacent nanoscale domains in MoSe$_2$ monolayers and reveals significant inhomogeneity where more commonly used confocal Raman microscopy would see a uniform distribution of spectra.

Although both the poly- and monocrystalline TERS maps show both the resonant and nonresonant spectra, the polycrystalline TERS map (inset of Figure 2a) also shows lines running parallel to the crystal edges where the TERS intensity drops dramatically (the horizontal black lines are the result of the probe picking up some contamination and losing the enhancement as a consequence). To further investigate these features, similar measurements were performed with a sharper SPM tip on a cleaner flake. Shown in Figure 3a−c are concurrently taken topography, CPD, and $\partial^2 C/\partial z^2$ (obtained from frequency-modulated SKPM measurements) maps of a
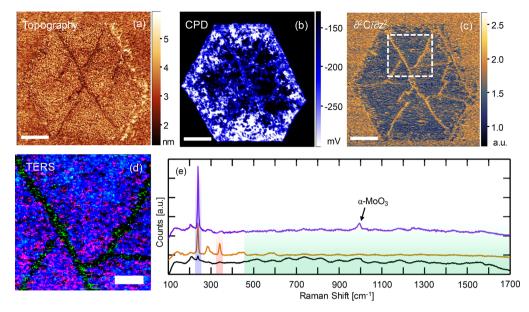
Figure 3. (a−c) Topography, contact potential difference (CPD), and $\partial^2 C/\partial z^2$ of a polycrystalline monolayer $MoSe_2$ flake transferred to gold. Scale bar is 1 μm. (d) Combined TERS maps of the white box in part c. Intensity of three different features are illustrated by color: 240 cm^{-1} (blue), 340 cm^{-1} (red), and the background signal spanning 450−1750 cm^{-1} (green). The relative intensities of the peaks represented by the colors are rescaled to clearly demonstrate the presence of nanoscale domains where the less intense peaks show considerable variation. The pattern of the GBs is identical to that revealed in the topography, CPD, and capacitance images. Scale bar is 300 nm. (e) Averaged TERS spectra showing resonant response (orange), nonresonant response (purple), and from the GB regions (black, showing significantly decreased intensity of Raman signal of $MoSe_2$ over the GBs). The features used to make the TERS map in part d are also highlighted with their respective color. Note that the resonant spectrum shows an additional peak at 995 cm^{-1}, which we attribute to MoO_3.

similar polycrystalline $MoSe_2$ flake, all of which clearly show internal features that are aligned with the crystal edges. [The roughness of the underlying gold substrate is about 1 nm (see the Supporting Information section F).] In the $\partial^2 C/\partial z^2$ maps, which show data that is proportional to the capacitance between the SPM tip and the sample (see the Supporting Information section G), we observe these features to have capacitance similar to the Au substrate, which is significantly higher than the $MoSe_2$ crystal, indicating that these could be regions where the $MoSe_2$ has been etched away along grain boundaries (GBs).
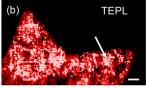
A higher-resolution TERS map was also collected, over just the white boxed area in Figure 3c (see Figure 3d). As before, we distinctly observe both resonant and nonresonant spectra (respectively, orange and purple in Figure 3e). The TERS map also reveals that the peaks corresponding to $MoSe_2$ (blue and red in the map) nearly vanish over the regions where the capacitance matches that of the substrate, and instead show only an increase in background signal (green). These observations support the conclusion that hot NaOH etches the polycrystalline $MoSe_2$ flakes along its GBs and exposes the underlying surface, but leaves monocrystalline flakes intact. By contrast, as-grown flakes allowed to age in air for 2 weeks demonstrated significantly increased topology at the GBs and edges, possibly due to oxidation (see the Supporting Information section H).

Regarding the origin of the two types of Raman signatures, we note that the resonant spectra with a significantly enhanced E′ peak is expected for a red excitation laser,[43] attributed to increased coupling of longitudinal phonons with the A and B excitons. Decreased intensity of this peak in the nonresonant spectra may suggest that the resonance conditions in these areas were suppressed due to doping variations or varied defect concentrations. This is further supported by the presence of a

new peak at 995 cm^{-1} in the nonresonant spectra in Figure 3e, which we attribute to nanoscale domains of MoO_3 that not only act as defect sites but can locally dope the $MoSe_2$ as well. The vibrational mode at 995 cm^{-1} is a well-known Raman peak for α-MoO_3 and corresponds to the stretching of the out-of-plane molybdenyl bond that gives α-MoO_3 its layered structure;[36,44−46] furthermore we have observed significant TERS enhancement of this peak alone in samples of α-MoO_3 prepared by vapor phase transfer (see the Supporting Information section I). While we cannot presently determine if these oxide domains exist from growth or are a result of exposure to air or NaOH, we can conclude that nanoscale domains of MoO_3 must exist within the transferred $MoSe_2$ flakes.

It is worth noting that such observations require the use of subwavelength imaging spectroscopic techniques, which in the case of the gap-mode regime can provide spatial resolution in TERS maps at the level of a few nanometers over regions tens of microns across in ambient conditions. In conventional confocal Raman microscopy, where the spot size of the laser is ~0.5 μm, the Raman signal of the boundaries and adjacent material would be averaged over this larger spatial scale (see the Supporting Information section J). By contrast, transmission electron microscopy (TEM), while able to possibly resolve defects at the atomic level, can typically only image regions no larger than 50 × 50 nm and risk missing sparse defects. That notwithstanding, in our own TEM analysis, we do not observe any vacancies (see the Supporting Information section K), nor do we observe a previously reported[47] Se vacancy defect peak at 250 cm^{-1} in our TERS spectra, indicating that the nanoscale inhomogeneities in our samples are not related to vacancies.

Employment of subwavelength spectroscopy can also be used for tip-enhanced photoluminescence (TEPL), and Figure 4a shows emission spectra extending to the range where the
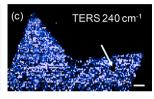
Figure 4. (a) Typical spectra showing coexistence of the TEPL and TERS (orange and purple) and a spectrum (black) from the location marked with white arrows in the maps where the TERS response was dramatically suppressed, though the PL and photocurrent signals retained significant intensity. (b, c) TEPL and TERS (240 cm^{-1} intensity) maps highlighting a region with strong TEPL and low TERS signals. Scale bar in the maps is 200 nm.
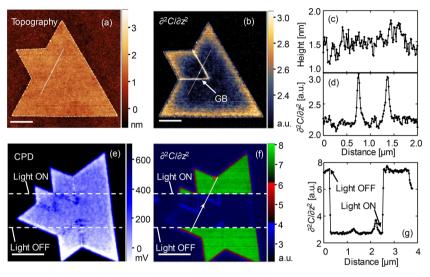

Figure 5. As-grown monolayer MoSe$_2$ on Si/SiO$_2$. (a) Topography and (b) $\partial^2 C/\partial z^2$ maps of a flake. Scale bars are 1 μm. (c, d) Topography and $\partial^2 C/\partial z^2$ cross sections along the white lines in parts a and b. Topography is completely featureless, while the GBs stand out extremely well in the capacitance image. (e, f) CPD and $\partial^2 C/\partial z^2$ of another flake on the same substrate taken in the dark and under illumination with a 638 nm laser at 75 μW. In the middle of the scan the illumination was turned off which resulted in immediate drop of the capacitance signal. Scale bars are 2 μm. (g) $\partial^2 C/\partial z^2$ along the line in part f, showing the greatly increased capacitance of the MoSe$_2$ while under illumination.

photoluminescence can be observed in addition to the Raman (TERS) signal. Strong TEPL response from MoSe$_2$ on gold is seen (Figure 4b), even though the flake was in good electric contact with the substrate (confirmed by significant photocurrent recorded simultaneously with these maps, see the Supporting Information section L). Contact of a 2D semiconductor with metallic[48] or even another semiconductor surface[33] can strongly quench PL emission. In our case, the TEPL signal exceeded the far-field PL by almost an order of magnitude, though the area from which the TEPL signal is collected (<400−600 nm^2) was almost 3 orders of magnitude smaller compared to the area from which the far-field PL signal was collected (in our case about 0.35 μm^2). The strength of the emission reflects field enhancement effects that increase both the coupling of the pump laser to the sample and the rate of radiative emission.

The position of the TEPL emission feature varied from 799 to 809 nm within the map. TERS and TEPL signals coexisted across most of the imaged area, though we found several locations (about 100 nm across) in which strong TEPL and significant photocurrent were observed with very low TERS signal. Because the pixel size in these TERS/TEPL maps is ∼17 nm, we can conclude that the observed preferential enhancement of TEPL and suppression of TERS was not an arbitrary event, but rather reflects specific properties of nanoscale domains.

Finally, we turn to SPM measurements on as-grown samples on SiO$_2$/Si to further explore the properties of GBs. Surprisingly, $\partial^2 C/\partial z^2$ imaging highlights otherwise invisible GBs, even in cases where topography of the inner parts of the polycrystalline flakes was completely featureless. In Figure 5a−d we see increased capacitance of the GBs and their somewhat counterintuitive shape protruding into the body of the MoSe$_2$ sample, instead of being positioned along the edge of the larger triangle. This behavior was observed in multiples flakes, even though the topography images suggest a flat, uniform surface (Figure 5a,c).

Performing SPM characterization in an instrument coupled to a Raman spectrometer has a further unique advantage in that surface potential, capacitance, conductivity, etc. can be measured in the dark and under illumination. Using this capability, we explore how capacitance and the surface potential of as-grown flakes change as a result of illumination with a 638 nm laser (∼75 μW, the same illumination conditions as in TERS experiments). While the GBs are only barely discernible in the CPD image, a dramatic increase of the capacitance was observed when the laser was turned on (Figure 5e−g). Turning the illumination off immediately resulted in a decrease of the capacitance signal and relatively little change in the surface potential. We also note that a slight increase of the capacitance was observed in the vicinity of the flake edges, which could be indicative of metallic edge states in 1L TMDs.[49]

We attribute the observed increase of the $\partial^2 C/\partial z^2$ signal over the grain boundaries to significantly increased charge carrier concentration in these regions, which is in good agreement with observations from Ma et al. detailing the metallic nature of twin grain boundaries in MoSe$_2$ at room temperature.[50] Enhancement of the $\partial^2 C/\partial z^2$ signal in response to illumination, which increases the concentration of charge carriers, also corroborates the conclusion that variations of this signal represent the variations of the charge carrier concentration. We thus affirm that, in as-grown MoSe$_2$, the concentration of charge carriers is significantly increased over the (possibly metallic) GBs, as well as along the outer edges of the flakes. The latter phenomenon is to some extent the opposite compared to what was observed in WS$_2$ flakes where the decrease of the PL signal and corresponding increase of TERS signal in the vicinity of the edges of the as-grown flakes were attributed to the decreased concentration of charge carriers.[51]

CONCLUSIONS

In summary, MoSe$_2$ monolayers were grown in high density with crystal sizes ranging from a few μm to 100 μm. We demonstrated the importance of comprehensive SPM characterization which, in addition to commonly collected topography, included surface potential and $\partial^2 C/\partial z^2$ imaging. $\partial^2 C/\partial z^2$ images of fresh, as-grown polycrystalline monolayer flakes with near-perfect topography very clearly showed the presence of grain boundaries which were protruding toward the center of the flakes, rather than being located along the edges of the main body of the crystal. Analysis of samples aged in ambient conditions for 2 weeks showed that significant degradation occurred along these grain boundaries, with appearance of new features in the surface potential images of aged flakes.

Correlation of this advanced SPM characterization with TERS and TEPL imaging revealed a number of unexpected features in MoSe$_2$ monolayers transferred to gold substrates in the form of nanoscale inhomogeneity in domains as small as few tens of nanometers. Two types of TERS spectra were observed, a nonresonant spectrum with a single dominant peak at 240 cm^{-1}, and another more common, resonant type also exhibiting fairly intense peaks at 287 and 340 cm^{-1}, as well as complex overtone peaks around 460 and 550 cm^{-1}. The size of the domains with correspondingly nonresonant or resonant response was several tens of nm, which makes these domains unobservable with conventional confocal Raman microscopy. By comparing our TERS measurements of MoSe$_2$ to α-MoO$_3$, we conclude that nanoscale inclusions of MoO$_3$ in the MoSe$_2$ matrix are responsible for these differences.

Furthermore, the intensity of TERS response was greatly suppressed at GBs of crystals transferred to gold, which we attribute to complete removal of MoSe$_2$ over these GBs either in the process of etching the underlying SiO$_2$ layer in hot NaOH solution during transfer to gold, or by fast degradation of the grain boundaries in ambient conditions. This observation as well as partial oxidation of nanoscale domains in MoSe$_2$ imply that the transfer process of transition metal diselenides from the growth substrate with strong bases may degrade the original properties of as-grown TMD crystals. Future work along these lines should involve employing gentler transfer techniques to explore how defects of known concentrations affect the nanoscale properties of monolayer semiconductors.

Comprehensive SPM characterization of TMDs both as-grown and transferred to Au substrates, combined with nanoscale spectroscopic characterization, offers an avenue for simple and noninvasive insights into the structure and properties of 2D semiconductors at a submicron scale. Broader use of these techniques can bridge the gap between atomic resolution imaging such as TEM and conventional optical microscopy and macroscopic characterization techniques, providing important information on both the structure and physical properties of TMDs at all relevant scales.

ASSOCIATED CONTENT

⑤ Supporting Information

The Supporting Information is available free of charge on the ACS Publications website at DOI: 10.1021/acsanm.7b00083.

    MoSe$_2$ growth details, XPS spectra, SPM and TERS instrumentation, MoSe$_2$ transfer process, reproducibility of TERS mapping, additional grain boundary CPD and TERS data, grain boundaries of aged flakes, Raman and TERS of α-MoO$_3$, mapping with confocal Raman spectroscopy, TEM imaging of transferred MoSe$_2$, and photocurrent measurements (PDF)

AUTHOR INFORMATION

Corresponding Author

*E-mail: epop@stanford.edu.

ORCID 🄾

Kirby K. H. Smithe: 0000-0003-2810-295X
Eilam Yalon: 0000-0001-7965-459X
Miguel Muñoz Rojo: 0000-0001-9237-4584
Eric Pop: 0000-0003-0436-8534

Author Contributions

○K.K.H.S. and A.V.K. contributed equally to this work.

Notes

The authors declare no competing financial interest.

REFERENCES

(1) Mak, K. F.; Shan, J. Photonics and Optoelectronics of 2D Semiconductor Transition Metal Dichalcogenides. *Nat. Photonics* **2016**, *10*, 216−226.

(2) Mak, K. F.; Lee, C.; Hone, J.; Shan, J.; Heinz, T. F. Atomically Thin MoS$_2$: A New Direct-Gap Semiconductor. *Phys. Rev. Lett.* **2010**, *105*, 136805.

(3) Splendiani, A.; Sun, L.; Zhang, Y.; Li, T.; Kim, J.; Chim, C. Y.; Galli, G.; Wang, F. Emerging Photoluminescence in Monolayer MoS$_2$. *Nano Lett.* **2010**, *10*, 1271−1275.

(4) Macneill, D.; Heikes, C.; Mak, K. F.; Anderson, Z.; Kormányos, A.; Zólyomi, V.; Park, J.; Ralph, D. C. Breaking of Valley Degeneracy

by Magnetic Field in Monolayer MoSe$_2$. *Phys. Rev. Lett.* **2015**, *114*, 037401.

(5) Xiao, D.; Liu, G.; Bin; Feng, W.; Xu, X.; Yao, W. Coupled Spin and Valley Physics in Monolayers of MoS$_2$ and Other Group-VI Dichalcogenides. *Phys. Rev. Lett.* **2012**, *108*, 196802.

(6) Zeng, H.; Dai, J.; Yao, W.; Xiao, D.; Cui, X. Valley Polarization in MoS$_2$ Monolayers by Optical Pumping. *Nat. Nanotechnol.* **2012**, *7*, 490−493.

(7) Mak, K. F.; He, K.; Shan, J.; Heinz, T. F. Control of Valley Polarization in Monolayer MoS$_2$ by Optical Helicity. *Nat. Nanotechnol.* **2012**, *7*, 494−498.

(8) Flatten, L. C.; He, Z.; Coles, D. M.; Trichet, A. A. P.; Powell, A. W.; Taylor, R. A.; Warner, J. H.; Smith, J. M. Room-Temperature Exciton-Polaritons with Two-Dimensional WS$_2$. *Sci. Rep.* **2016**, *6*, 33134.

(9) Ugeda, M. M.; Bradley, A. J.; Shi, S.-F.; da Jornada, F. H.; Zhang, Y.; Qiu, D. Y.; Ruan, W.; Mo, S.-K.; Hussain, Z.; Shen, Z.-X.; Wang, F.; Louie, S. G.; Crommie, M. F. Giant Bandgap Renormalization and Excitonic Effects in a Monolayer Transition Metal Dichalcogenide Semiconductor. *Nat. Mater.* **2014**, *13*, 1091−1095.

(10) Mak, K. F.; He, K.; Lee, C.; Lee, G. H.; Hone, J.; Heinz, T. F.; Shan, J. Tightly Bound Trions in Monolayer MoS$_2$. *Nat. Mater.* **2013**, *12*, 207−211.

(11) Palummo, M.; Bernardi, M.; Grossman, J. C. Exciton Radiative Lifetimes in Two-Dimensional Transition Metal Dichalcogenides. *Nano Lett.* **2015**, *15*, 2794−2800.

(12) Arora, A.; Nogajewski, K.; Molas, M. R.; Koperski, M.; Potemski, M. Exciton Band Structure in Layered MoSe$_2$: From a Monolayer to the Bulk Limit. *Nanoscale* **2015**, *7*, 20769−20775.

(13) Chang, Y.; Zhang, O. W.; Zhu, O. Y.; Han, Y.; Pu, J.; Chang, J.; Hsu, W. Monolayer MoSe$_2$ Grown by Chemical Vapor Deposition for Fast Photodetection. *ACS Nano* **2014**, *8*, 8582−8590.

(14) Zhang, Y.; Chang, T.-R.; Zhou, B.; Cui, Y.-T.; Yan, H.; Liu, Z.; Schmitt, F.; Lee, J.; Moore, R.; Chen, Y.; Lin, H.; Jeng, H.-T.; Mo, S.-K.; Hussain, Z.; Bansil, A.; Shen, Z.-X. Direct Observation of the Transition from Indirect to Direct Bandgap in Atomically Thin Epitaxial MoSe$_2$. *Nat. Nanotechnol.* **2014**, *9*, 111−115.

(15) Shaw, J. C.; Zhou, H.; Chen, Y.; Weiss, N. O.; Liu, Y.; Huang, Y.; Duan, X. Chemical Vapor Deposition Growth of Monolayer MoSe$_2$ Nanosheets. *Nano Res.* **2014**, *7*, 511−517.

(16) Lu, X.; Utama, M. I. B.; Lin, J.; Gong, X.; Zhang, J.; Zhao, Y.; Pantelides, S. T.; Wang, J.; Dong, Z.; Liu, Z.; Zhou, W.; Xiong, Q. Large-Area Synthesis of Monolayer and Few-Layer MoSe$_2$ Films on SiO$_2$ Substrates. *Nano Lett.* **2014**, *14*, 2419−2425.

(17) Xia, J.; Huang, X.; Liu, L.-Z.; Wang, M.; Wang, L.; Huang, B.; Zhu, D.-D.; Li, J.-J.; Gu, C.-Z.; Meng, X.-M. CVD Synthesis of Large-Area, Highly Crystalline MoSe$_2$ Atomic Layers on Diverse Substrates and Application to Photodetectors. *Nanoscale* **2014**, *6*, 8949−8955.

(18) Wang, X.; Gong, Y.; Shi, G.; Chow, W. L.; Keyshar, K.; Ye, G.; Vajtai, R.; Lou, J.; Liu, Z.; Ringe, E.; Tay, B. K.; Ajayan, P. M. Chemical Vapor Deposition Growth of Crystalline Monolayer MoSe$_2$. *ACS Nano* **2014**, *8*, 5125−5131.

(19) Pradhan, N. R.; Rhodes, D.; Xin, Y.; Memaran, S.; Bhaskaran, L.; Siddiq, M.; Hill, S.; Ajayan, P. M.; Balicas, L. Ambipolar Molybdenum Diselenide Field-Effect Transistors: Field-Effect and Hall Mobilities. *ACS Nano* **2014**, *8*, 7923−7929.

(20) Larentis, S.; Fallahazad, B.; Tutuc, E. Field-Effect Transistors and Intrinsic Mobility in Ultra-Thin MoSe$_2$ Layers. *Appl. Phys. Lett.* **2012**, *101*, 223104.

(21) Verma, P. Tip-Enhanced Raman Spectroscopy: Technique and Recent Advances. *Chem. Rev.* **2017**, *117*, 6447−6466.

(22) Saunin, S. A.; Krayev, A. V.; Zhizhimontov, V. V.; Gavrilyuk, V. V.; Grigorov, L. N.; Belyaev, A. V.; Evplov, D. A. Systems and Methods for Non-Destructive Surface Chemical Analysis of Samples. *U.S. Patent* 9,568,495 B2, 2017.

(23) Su, W.; Roy, D. Visualizing Graphene Edges Using Tip-Enhanced Raman Spectroscopy. *J. Vac. Sci. Technol., B: Nanotechnol. Microelectron.: Mater., Process., Meas., Phenom.* **2013**, *31*, 041808.

(24) Beams, R.; Cançado, L. G.; Jorio, A.; Vamivakas, A. N.; Novotny, L. Tip-Enhanced Raman Mapping of Local Strain in Graphene. *Nanotechnology* **2015**, *26*, 175702.

(25) Stadler, J.; Schmid, T.; Zenobi, R. Nanoscale Chemical Imaging of Single-Layer Graphene. *ACS Nano* **2011**, *5*, 8442−8448.

(26) Su, W.; Kumar, N.; Mignuzzi, S.; Crain, J.; Roy, D. Nanoscale Mapping of Excitonic Processes in Single-Layer MoS$_2$ Using Tip-Enhanced Photoluminescence Microscopy. *Nanoscale* **2016**, *8*, 10564−10569.

(27) Bao, W.; Borys, N. J.; Ko, C.; Suh, J.; Fan, W.; Thron, A.; Zhang, Y.; Buyanin, A.; Zhang, J.; Cabrini, S.; Ashby, P. D.; Weber-Bargioni, A.; Tongay, S.; Aloni, S.; Ogletree, D. F.; Wu, J.; Salmeron, M. B.; Schuck, P. J. Visualizing Nanoscale Excitonic Relaxation Properties of Disordered Edges and Grain Boundaries in Monolayer Molybdenum Disulfide. *Nat. Commun.* **2015**, *6*, 7993.

(28) Park, K. D.; Khatib, O.; Kravtsov, V.; Clark, G.; Xu, X.; Raschke, M. B. Hybrid Tip-Enhanced Nanospectroscopy and Nanoimaging of Monolayer WSe$_2$ with Local Strain Control. *Nano Lett.* **2016**, *16*, 2621−2627.

(29) Zhang, Y.; Voronine, D. V.; Qiu, S.; Sinyukov, A. M.; Hamilton, M.; Liege, Z.; Sokolov, A. V.; Zhang, Z.; Scully, M. O. Improving Resolution in Quantum Subnanometre-Gap Tip-Enhanced Raman Nanoimaging. *Sci. Rep.* **2016**, *6*, 25788.

(30) Voronine, D. V.; Lu, G.; Zhu, D.; Krayev, A. Tip-Enhanced Raman Scattering of MoS$_2$. *IEEE J. Sel. Top. Quantum Electron.* **2017**, *23*, 138.

(31) Rahaman, M.; Rodriguez, R. D.; Plechinger, G.; Moras, S.; Schüller, C.; Korn, T.; Zahn, D. R. T. Highly Localized Strain in a MoS$_2$/Au Heterostructure Revealed by Tip-Enhanced Raman Spectroscopy. *Nano Lett.* **2017**, *17*, 6027−6033.

(32) Kastl, C.; Chen, C. T.; Kuykendall, T.; Shevitski, B.; Darlington, T. P.; Borys, N. J.; Krayev, A.; Schuck, P. J.; Aloni, S.; Schwartzberg, A. M. The Important Role of Water in Growth of Monolayer Transition Metal Dichalcogenides. *2D Mater.* **2017**, *4*, 021024.

(33) Ling, X.; Lee, Y.-H.; Lin, Y.; Fang, W.; Yu, L.; Dresselhaus, M. S.; Kong, J. Role of the Seeding Promoter in MoS$_2$ Growth by Chemical Vapor Deposition. *Nano Lett.* **2014**, *14*, 464−472.

(34) Smithe, K. K. H.; English, C. D.; Suryavanshi, S. V.; Pop, E. Intrinsic Electrical Transport and Performance Projections of Synthetic Monolayer MoS$_2$ Devices. *2D Mater.* **2017**, *4*, 011009.

(35) Tran, M. D.; Kim, J. H.; Lee, Y. H. Tailoring Photoluminescence of Monolayer Transition Metal Dichalcogenides. *Curr. Appl. Phys.* **2016**, *16*, 1159−1174.

(36) Julien, C.; Khelfa, A.; Hussain, O.; Nazri, G. Synthesis and Characterization of Flash-Evaporated MoO$_3$ Thin Films. *J. Cryst. Growth* **1995**, *156*, 235−244.

(37) Li, Y.; Chernikov, A.; Zhang, X.; Rigosi, A.; Hill, H. M.; Van Der Zande, A. M.; Chenet, D. A.; Shih, E. M.; Hone, J.; Heinz, T. F. Measurement of the Optical Dielectric Function of Monolayer Transition-Metal Dichalcogenides: MoS$_2$, MoSe$_2$, WS$_2$, and WSe$_2$. *Phys. Rev. B: Condens. Matter Mater. Phys.* **2014**, *90*, 205422.

(38) Amani, M.; Chin, M. L.; Mazzoni, A. L.; Burke, R. A.; Najmaei, S.; Ajayan, P. M.; Lou, J.; Dubey, M. Growth-Substrate Induced Performance Degradation in Chemically Synthesized Monolayer MoS$_2$ Field Effect Transistors. *Appl. Phys. Lett.* **2014**, *104*, 203506.

(39) Chen, C.; Hayazawa, N.; Kawata, S. A 1.7 nm Resolution Chemical Analysis of Carbon Nanotubes by Tip-Enhanced Raman Imaging in the Ambient. *Nat. Commun.* **2014**, *5*, 3312.

(40) Picardi, G.; Chaigneau, M.; Ossikovski, R.; Licitra, C.; Delapierre, G. Tip Enhanced Raman Spectroscopy on Azobenzene Thiol Self-Assembled Monolayers on Au(111). *J. Raman Spectrosc.* **2009**, *40*, 1407−1412.

(41) Deckert-Gaudig, T.; Deckert, V. Tip-Enhanced Raman Scattering Studies of Histidine on Novel Silver Substrates. *J. Raman Spectrosc.* **2009**, *40*, 1446−1451.

(42) Deckert-Gaudig, T.; Bailo, E.; Deckert, V. Tip-Enhanced Raman Scattering (TERS) of Oxidised Glutathione on an Ultraflat Gold Nanoplate. *Phys. Chem. Chem. Phys.* **2009**, *11*, 7360−7362.

(43) Soubelet, P.; Bruchhausen, A. E.; Fainstein, A.; Nogajewski, K.; Faugeras, C. Resonance Effects in the Raman Scattering of Mono- and Few Layers MoSe$_2$. *Phys. Rev. B: Condens. Matter Mater. Phys.* **2016**, *93*, 155407.

(44) Koike, K.; Wada, R.; Yagi, S.; Harada, Y.; Sasa, S.; Yano, M. Characteristics of MoO$_3$ Films Grown by Molecular Beam Epitaxy. *Jpn. J. Appl. Phys.* **2014**, *53*, 05FJ02.

(45) Sivakumar, R.; Sanjeeviraja, C.; Jayachandran, M.; Gopalakrishnan, R.; Sarangi, S. N.; Paramanik, D.; Som, T. MeV N +-Ion Irradiation Effects on α-MoO$_3$ Thin Films. *J. Appl. Phys.* **2007**, *101*, 034913.

(46) Illyaskutty, N.; Sreedhar, S.; Sanal Kumar, G.; Kohler, H.; Schwotzer, M.; Natzeck, C.; Pillai, V. P. M. Alteration of Architecture of MoO$_3$ Nanostructures on Arbitrary Substrates: Growth Kinetics, Spectroscopic and Gas Sensing Properties. *Nanoscale* **2014**, *6*, 13882−13894.

(47) Mahjouri-Samani, M.; Liang, L.; Oyedele, A.; Kim, Y. S.; Tian, M.; Cross, N.; Wang, K.; Lin, M. W.; Boulesbaa, A.; Rouleau, C. M.; Puretzky, A. A.; Xiao, K.; Yoon, M.; Eres, G.; Duscher, G.; Sumpter, B. G.; Geohegan, D. B. Tailoring Vacancies Far beyond Intrinsic Levels Changes the Carrier Type and Optical Response in Monolayer MoSe$_{2-X}$ Crystals. *Nano Lett.* **2016**, *16*, 5213−5220.

(48) Bhanu, U.; Islam, M. R.; Tetard, L.; Khondaker, S. I. Photoluminescence Quenching in Gold - MoS$_2$ Hybrid Nanoflakes. *Sci. Rep.* **2015**, *4*, 05575.

(49) Zhang, C.; Johnson, A.; Hsu, C.-L.; Li, L.-J.; Shih, C.-K. Direct Imaging of Band Profile in Single Layer MoS$_2$ on Graphite: Quasiparticle Energy Gap, Metallic Edge States, and Edge Band Bending. *Nano Lett.* **2014**, *14*, 2443−2447.

(50) Ma, Y.; Kolekar, S.; Coy Diaz, H.; Aprojanz, J.; Miccoli, I.; Tegenkamp, C.; Batzill, M. Metallic Twin Grain Boundaries Embedded in MoSe$_2$ Monolayers Grown by Molecular Beam Epitaxy. *ACS Nano* **2017**, *11*, 5130−5139.

(51) Yu, Y.; Hu, S.; Su, L.; Huang, L.; Liu, Y.; Jin, Z.; Alexander, A.; Geohegan, D. B.; Kim, K. W.; Zhang, Y.; Cao, L. Equally Efficient Interlayer Exciton Relaxation and Improved Absorption in Epitaxial and Non-Epitaxial MoS$_2$ /WS$_2$ Heterostructures. *Nano Lett.* **2015**, *15*, 486−491.

Nanoscale Heterogeneities in Monolayer MoSe₂ Revealed by Correlated Scanning Probe Microscopy and Tip-Enhanced Raman Spectroscopy

Kirby K. H. Smithe[1†], Andrey V. Krayev[2†], Connor S. Bailey[1], Hye Ryoung Lee[1,3], Eilam Yalon[1], Özgür Burak Aslan[4,5], Miguel Muñoz Rojo[1], Sergiy Krylyuk[6,7], Payam Taheri[6,8], Albert V. Davydov[6], Tony F. Heinz[4,5], and Eric Pop[1,3,9]*

[1]Department of Electrical Engineering, Stanford University, Stanford, CA 94305, USA

[2]Horiba Scientific, Novato, CA 94949, USA

[3]Department of Materials Science & Engineering, Stanford University, Stanford, CA 94305, USA

[4]Department of Applied Physics, Stanford University, Stanford, CA 94305, USA

[5]SLAC National Accelerator Laboratory, Menlo Park, CA 94025, USA

[6]Material Measurement Laboratory, National Institute of Standards and Technology, Gaithersburg, MD 20899, USA

[7]Theiss Research, Inc., La Jolla, CA 92037, USA

[8]ASRC Federal at NASA, Seabrook, MD 20706, USA

[9]Precourt Institute for Energy, Stanford University, Stanford, CA 94305, USA

†Authors contributed equally to this work.

*Author to whom correspondence should be addressed: epop@stanford.edu

A. MoSe₂ Growth Details

For the MoSe₂ flakes studied in the main text, experimental details are as follows. ~100 mg worth of solid Se pellets was placed upstream in an alumina boat, and a very small amount (~0.1 mg) of MoO₃ was placed in an alumina boat at the center of the furnace, with 10 inches separating the precursors. After growth substrates were treated with HMDS, ~25 μL worth of 100 μM perylene-3,4,9,10 tetracarboxylic acid tetrapotassium salt (PTAS) was pipetted in several drops around the substrate edges. After drying the PTAS on a hot plate in air (~70°C), the substrate was placed face-down on the crucible over the MoO₃. The growth recipe is:

1) Pump the tube to base pressure (~100 mTorr)
2) Ramp tube to 400 °C in 5 min while flowing 1000 sccm Ar to reach 760 Torr
3) Ramp tube to 700 °C in 5 min while ramping sleeve to 500 °C and flowing 100 sccm Ar
4) Ramp tube to 800 °C in 5 min while holding sleeve at 500 °C and flowing 30 sccm Ar
5) Ramp tube to 850 °C in 5 min while holding sleeve at 500 °C and flowing 25/5 sccm Ar/H_2
6) Hold tube at 850 °C while holding sleeve at 500 °C for 30 min and flowing 25/5 sccm Ar/H_2
7) Kill power to furnace and heating sleeve and flow 1000 sccm Ar for 15 min, still at 760 Torr
8) Open throttle valve 100% and continue flowing 1000 sccm Ar for an additional 15 min
9) Once the tube is below 500 °C, open the hatch for rapid cooling
10) Flow 1000 sccm Ar to return to 760 Torr

Figure S1. Cartoon of the tube furnace illustrating placement of solid precursors and substrate.

Figure S2. Photograph of the PlanarTECH custom 2-inch tube furnace used to grow $MoSe_2$, corresponding to the diagram in Figure S1.

B. XPS Spectra

X-ray photoemission spectroscopy (XPS) was performed on samples grown on SiO_2 and also transferred to Au-coated substrates, shown below. Because the spot size of typical XPS measurements is ~100 μm, it is difficult for such measurements to detect the presence of sparse nanoscale defects.
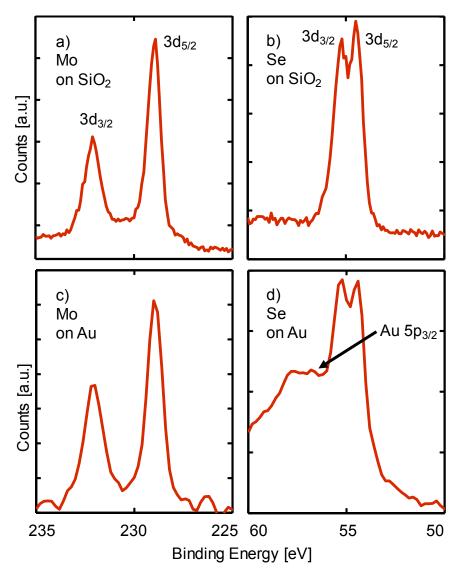

Figure S3. XPS spectra of the characteristics 3d peaks of Mo and Se, for $MoSe_2$ grown directly on SiO_2 [(a) and (b)] and transferred to Au-coated substrates [(c) and (d)]. The lack of higher energy peaks indicates the absence of species other than Mo^{4+} and Se^{2-}. The broad feature centered around 57 eV in (d) is the Au $5p_{3/2}$ peak.

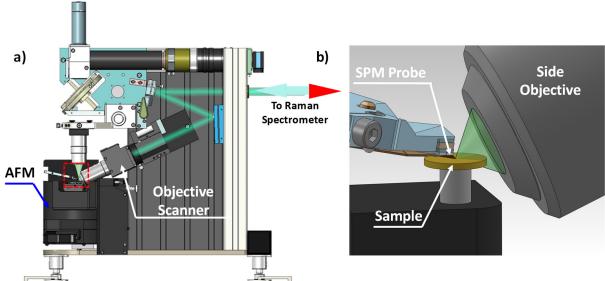## C. SPM and TERS Instrumentation

Figure S4. (a) Side view schematic of the SPM instrumentation setup from Horiba Scientific, showing the AFM stage, laser source, objective scanner, and optical path to the Raman spectrometer. (b) Zoomed-in view of the red box in (a), detailing sample placement on the AFM stage as well as the SPM probe coupled to the side objective.

D. MoSe$_2$ Transfer Process

Our transfer process is very similar to the standard PMMA-supported transfer techniques reported elsewhere. The process flow is as follows:

1) Drop-cast 950 PMMA A4 onto the growth substrate (just enough to completely cover it, typically one drop per cm^2 of substrate)
2) Cure PMMA on a hot plate at 150 °C for 10 minutes
3) Use a razor blade to remove PMMA from the very edges of the substrate
4) Float the substrate in 1M NaOH solution heated to 80 °C
5) Wait for the NaOH to dissolve the SiO$_2$, resulting in the growth substrate sinking while the PMMA/MoSe$_2$ remains floating on the surface
6) Use tweezers to transfer the rigid PMMA/MoSe$_2$ to a room-temperature bath of deionized water
7) Allow PMMA/MoSe$_2$ to float in DI H$_2$O 30 for minutes
8) Use tweezers to transfer the PMMA/MoSe$_2$ to the Au-coated target substrate
9) Use an N$_2$ gun to blow directly down onto the PMMA to push as much water as possible out from underneath
10) Place the substrate on a room-temperature hot plate and heat to 150 °C over a time of 20 minutes
11) Soak in acetone for an hour to remove most of the PMMA
12) Remove final PMMA residues by drop-casting acetone on the substrate for 60 seconds while it rotates in a spincoater at 3000 rpm
13) Perform a final rinse with methanol and dry with an N$_2$ gun

It is worth noting that, while complete removal of residues is likely impossible, the penultimate rinsing while the sample is rotating is an important step for sample preparation as it eliminates the possibility of formation of "puddles" of PMMA that form if the solvent is allowed to evaporate slowly, which forms multiple retracting menisci arbitrarily distributed across the sample surface.
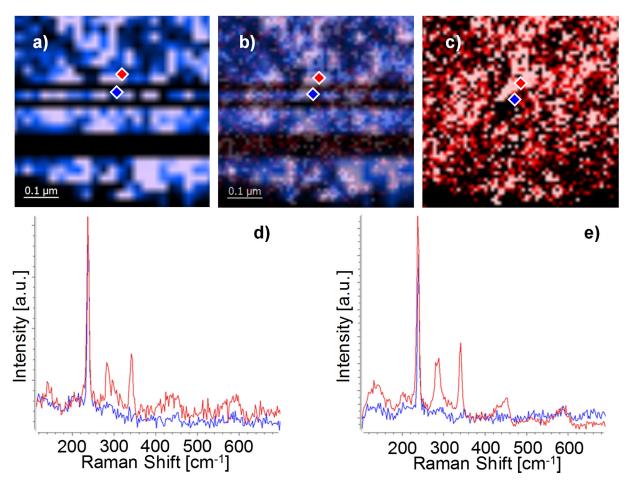
E. Reproducibility of TERS Mapping

Figure S5. (a) A portion of a TERS map from the inset of Figure 2(a) [showing the intensity map of the 240 cm^{-1} feature]. (b) The same area from the consecutively recorded TERS map [inset of Figure S6(e), showing the intensity of the 340 cm^{-1} feature] overlaid with 50% transparency over the map from Figure S5(a). (c) The same area, but only showing the TERS intensity of the 340 cm^{-1} feature from Figure S6(e). (d) and (e) The spectra from correspondingly colored locations in (a) and (c), respectively. The location of the domains with non-resonant [blue line] and resonant [red line] is nearly identical in both maps, showing that TERS measurements are reproducible over time.

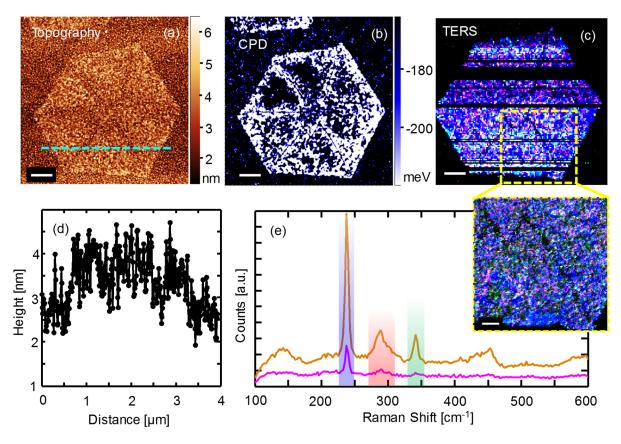## F. Grain Boundary CPD and TERS data of polycrystalline flakes transferred to gold

Figure S6. Topography (a), CPD (b), combined TERS map (c) images of a polycrystalline flake of MoSe$_2$ transferred to gold shown in Figure 2(a), showing all showing features running parallel to the crystal edges towards the center of the crystal. Scale bars in (a-c) are 500 nm. In (c), the colors represent the intensity of 240 cm^{-1} peak (blue), 287 cm^{-1} (red), and 340 cm^{-1} (green). (d) Topography cross-section of the cyan dotted line in Figure S6(a), showing the surface roughness of both the Au substrate and the transferred flakes to be about 1 nm. (e) Averaged TERS spectra from the GB (pink) and immediately adjacent (50 nm away, orange) areas of the flake showing significantly decreased intensity of Raman signal of MoSe$_2$ over the GBs. Inset: Combined TERS map (150 pixels per line) of the boxed yellow region in Figure S6(c), with higher spatial resolution and stability enhancement, also showing decreased intensity of TERS signal over the GBs. Scale bar is 200 nm. This TERS map had no imaging artifacts and nicely reproduced the shape of the GB observed in the CPD image and the previous, larger TERS map.

G. Capacitance Mapping

In a frequency-modulated SKPM measurement, the measured signal is proportional to a frequency shift, which is itself proportional to the vertical gradient of the capacitive force ($\nabla_z F$) between the SPM tip and the sample surface. The capacitive force itself is proportional to the gradient of

capacitive energy ($F = -\nabla U$), which is in turn proportional to the actual capacitance multiplied by some geometric factor ($U \propto C$). (Naïvely, for a parallel plate capacitor, $U = CV^2/2$, $F = CV^2/2z$, and so $\nabla_z F = -CV^2/2z^2$.) Thus the measured signal is still directly proportional to the capacitance of the sample/substrate. While the values we are showing are not direct measurements of capacitance in units of Farads, the relative change in the measurement of $\partial^2 C/\partial z^2$ is still proportional to the relative change in actual capacitance, which is why these maps are displayed in arbitrary units.

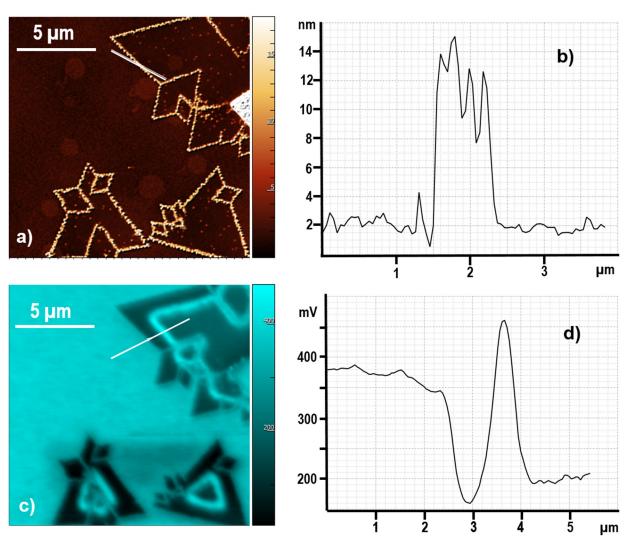## H. Grain Boundaries (GBs) of Aged Flakes

Figure S7. Topography image (a), corresponding section analysis (b), CPD image (c) and corresponding section analysis (d) of aged (two weeks) as-grown flakes of MoSe$_2$ on SiO$_2$/Si. Edges as well as the grain boundaries protruding into the flake body are significantly elevated (10-12 nm) over the flakes. Stripe of increased (+250 mV) surface potential following the contour of corresponding flakes was an interesting phenomenon that was not observed in freshly prepared flakes.

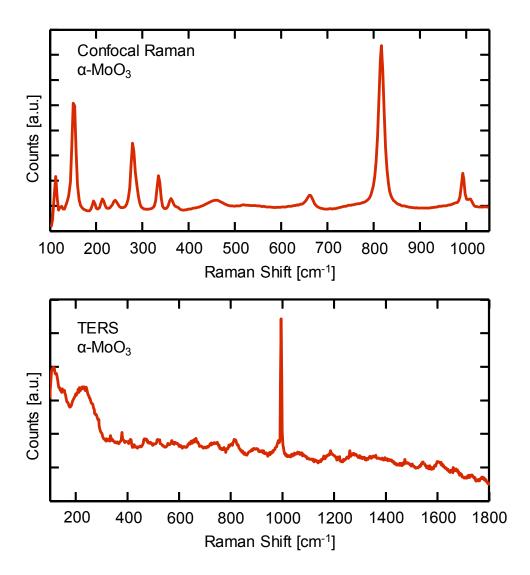## I. Raman and TERS spectra of exfoliated α-MoO₃ layer

Figure S8. Comparison of ordinary (top) and tip-enhanced (bottom) Raman spectra for α-MoO₃ monocrystalline layer. While many modes are visible in the regular configuration, only the out-of-plane molybdenyl bond peak at 995 cm⁻¹ is amplified in the TERS spectrum.
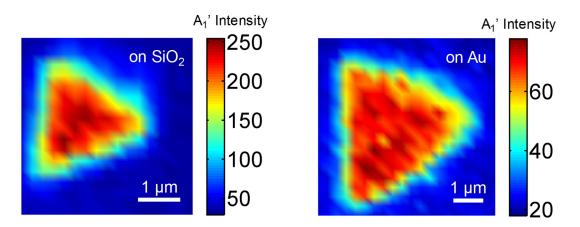
J. Mapping with Confocal Raman Spectroscopy

Figure S9. Intensity maps of the A_1' peak of MoSe$_2$ flakes grown on SiO$_2$ (step sizes of 250 nm) and transferred to Au (step sizes of 300 nm) taken with a 633 nm laser. While it is evident that the edges of the flakes show a different Raman response compared to the center, internal nanoscale inhomogeneity is difficult to discern due to the signal being averaged over areas of ~500 nm.
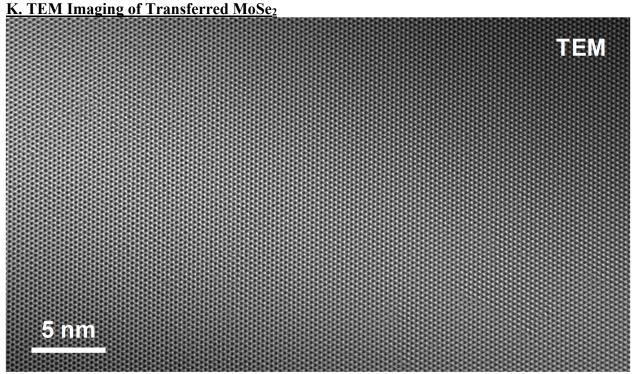
K. TEM Imaging of Transferred MoSe$_2$

Figure S10. TEM image of a monolayer MoSe$_2$ flake transferred to a TEM grid using hot NaOH. This image was taken at 300 kV by aberration-corrected TEM (FEI Titan FEI Titan 80-300 environmental transmission electron microscope) in monochromated mode. No vacancies or dislocations are observed at atomic sites, though substitution of other species such as oxygen is still possible, but would require the use of more advanced techniques to discern. It is also very possible that the ~200 nm^2 area imaged here simply does not capture any defects.
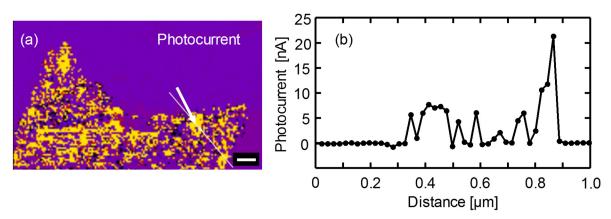
L. Photocurrent Measurements

Figure S11. (a) Photocurrent map taken concurrently with the TEPL and TERS maps shown in Figure 4. The patchy appearance of the photocurrent map could be caused by inevitable residual PMMA contamination that prevented good electric contact, while still preserving conditions for efficient TERS and TEPL. (b) Cross-section of the photocurrent map along the white line in (a).